Chemical templates that assemble the metal superhydrides

Yuanhui Sun
California State University Northridge
Maosheng Miao (mmiao@csun.edu)
California State University, Northridge https://orcid.org/0000-0001-9486-1204

Article

Keywords: chemical bonding, superconductors, computational chemistry

Posted Date: January 22nd, 2021

DOI: https://doi.org/10.21203/rs.3.rs-130093/v1

Chemical templates that assemble the metal superhydrides

Yuanhui Sun and Maosheng Miao*

Department of Chemistry and Biochemistry, California State University Northridge, CA USA

***Email: mmiao@csun.edu**

The recent incessant discoveries of high-pressure hydrides totally altered our road map toward finding room temperature superconductors. Especially, metal superhydrides consisting of hydrogen covalent networks that resemble metallic hydrogen are favorable candidates for improving T_c and lowering pressure. However, the dissociation of H_2 and the formation of H covalent network in superhydrides need a large chemical driving force that remains unexplained. Our high-throughput calculations show that, after removing H atoms, the remaining metal lattices exhibit unusual electron occupations at the interstitial regions, which matches excellently to the H lattice like a template. Furthermore, H lattices consist of 3D aromatic building units that are greatly stabilized by chemical templates of metals close to s-d boarder. This theory can help predicting ternary superhydrides that may form at lower pressure.

Among many remarkable physical and chemical properties of hydrogen, its capability of achieving superconducting state at or above room temperature has received intensive attention in condensed matter studies for many decades.[1–3] However, hydrogen is very resistive to metallization and polymerization that is an essential step toward superconductivity, and large driving forces are needed to overcome it. As predicted theoretically, a tremendous high pressure

of 550 GPa is needed to drive the transformation of hydrogen to atomic phases.[1,4,5] Therefore, the chemical forces that can "pre-compress" the hydrogen became an attractive approach of superconductive hydrogen under moderate pressure[2] and have led to the predictions and syntheses of numerous hydrogen-rich compounds that brought us ever close to room temperature superconductivity. These compounds can be roughly categorized into metal hydrides and non-metal hydrides. A latter type, H_3S showed a T_c of 203 K near 150 GPa,[6] which is the first to break the 25-year T_c record of cuperates. More profoundly, a ternary C-S-H system has just been demonstrated to become superconducting at about 15 °C and 267 GPa.[7] All H atoms in these compounds bond with p-block elements that are in hypervalent states.[8] In contrast, many metals close to the s-d boarder such as Ca, Sc, Y, La, Ce, Th incline to form superhydrides with exceedingly high H compositions in which all H atoms form extended lattices (Fig. 1a-c).[9–16] The H lattices in these compounds feature strong covalent bonding, high electron density and strong electron-phonon coupling, giving rise to superconductivity at very high temperatures.[17–19]

A large chemical driving force is needed to explain the formation of metal superhydrides. The available assumptions focus either at the volume effect or charge transfer between metals and hydrogen,[9,20] which can be examined by splitting the enthalpy changes into the changes of internal energy and the PV term (Fig. 1d-f and Supplementary Fig. 1). Generally, metallic hydrogen phases such as Cs-IV show significant volume reduction while comparing with molecular phases such as C_2/c, but their internal energies are much higher at lower pressures. The volume reductions are even more significant for many superhydrides. However, for most of the superhydrides, ΔPV increases with pressure. The volume of H in LaH_{10} becomes higher than Cs-IV H at about 170 GPa and even higher than molecular C_2/c phase at about 330 GPa.

Therefore, it cannot be a consistent driving force for the formation of superhydrides. The volume reduction is more of a result of strong chemical interactions with high symmetry constrains.

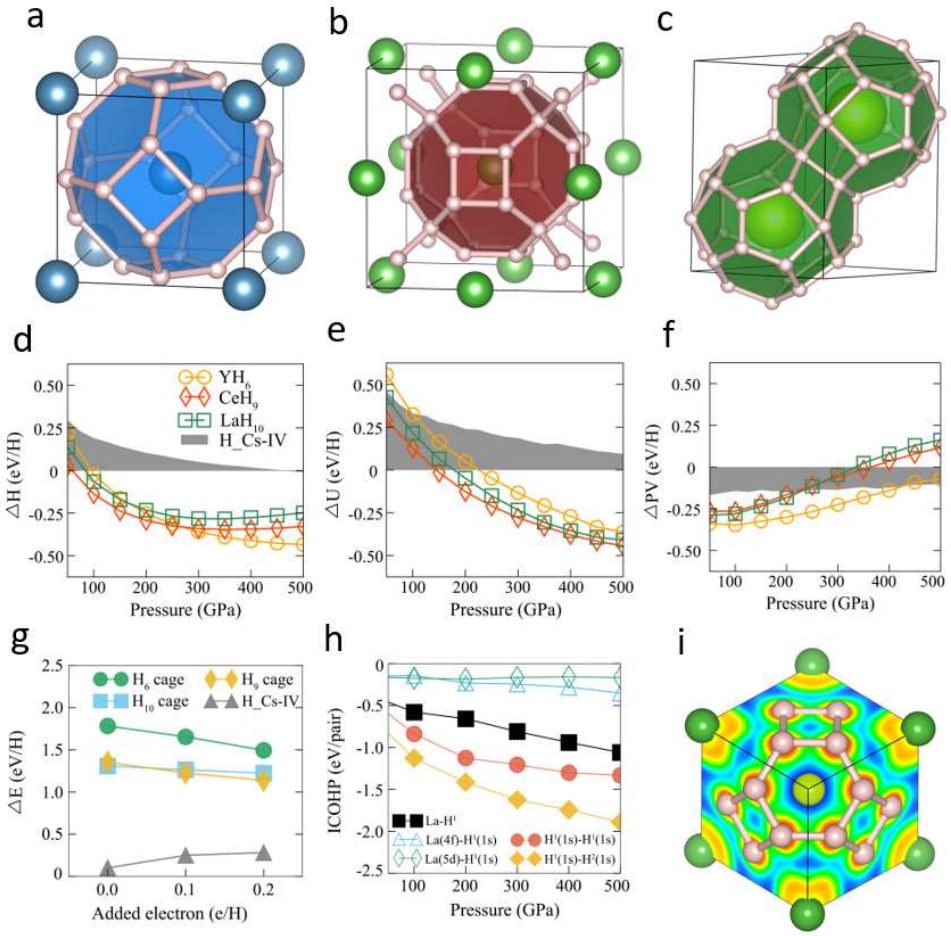

Fig. 1 | Structure, stability and bonding features of metal superhydrides. a-c, The sodalite structures of three major types of metal superhydrides, including CaH_6 in $Im\bar{3}m$ structure, LaH_{10} in $Fm\bar{3}m$ structure, and CeH_9 in $P6_3/mmc$ structure. The large blue, green and yellow balls represent the Ca, La, and Ce atoms; and the small white balls represent the H atoms. **d-f**, The extracted enthalpy (ΔH), internal energy (ΔU) and $P\Delta V$ term of hydrogen in superhydrides relative to pristine hydrogen in molecular phase as functions of pressure (Method). The shaded areas show ΔH, ΔU, and $P\Delta V$ of metallic H in Cs-IV structure. **g**, The internal energies of hydrogen lattices (after removing metal atoms from superhydridies) in CaH_6, LaH_{10}, and CeH_9 and of metallic hydrogen in Cs-IV structure relative to molecular hydrogen phase as functions of added charges. **h**, The integrated crystalline orbital Hamiltonian population (ICOHP) of La–H, La 5d – H^1 1s, La 4f – H^1 1s, H^1 – H^1, and H^1 – H^2 as functions of pressure. **i**, The electron localization function (ELF) of YH_6 at 300 GPa, viewed from (111) direction. A [111] cutoff plane is placed at a distance of 4.40 Å from the origin.

In contrast to PV, the relative internal energies of superhydrides decrease steadily while comparing with molecular and atomic hydrogen phases (Fig. 1e and Supplementary Fig. 1), indicating strong chemical interactions between H and metals. One theory attributes this chemical interaction to the charge doping from metals to H, which seemingly explains the destabilization of H_2 molecules because the extra electrons will occupy their anti-bonding states. However, calculations show that the excess charges also destabilize extended H lattices and the overall effect to H polymerization is insignificant (Fig. 1g). The energy of Cs-IV phase of metallic H[21,22] actually goes up comparing with H_2 C_2/c phase[23,24] while adding electrons (Fig. 1g). Furthermore, the charge doping from metal to hydrogen in superhydrides decreases with increasing pressure, distinctly opposing the trend of internal energy. Besides charge doping, the strong covalent bonding between metals and hydrogen seems to be another candidate of the driving force. However, both integrated Crystalline Orbital Hamiltonian Population (ICOHP)[25] (Fig. 1h) and Electron Localization Function (ELF)[26] (Fig. 1i) reveal that the M-H bond strengths are significantly weaker than H-H bonds and therefore can hardly cause the formation of extended H lattice. Especially, the very small ICOHP values between the 5d/4f orbitals of La and H 1s show that these orbitals do not play major roles in forming metal superhydrides. In the following sections, we will show that instead of directly bonding with H, the presence of the metals significantly enhances the stability of the extended hydrogen lattices in superhydrides through a chemical template effect.

Results and discussions

The conventional theory of chemical bonds in molecules and solid compounds take the consisting atoms as the initial states.[27] The charge transfer and the bond energies are obtained by

referring to free atoms and their quantum orbitals. While describing superhydrides MH_n, it is advantageous to take the sub-lattices, including metal and H_n lattices respectively, as the starting points. A study of the sub-lattices will reveal pre-existing features of the electronic structure before forming metal superhydrides, which turns out to be essential for apprehending the mechanism of superhydride formation. In the following, we will employ high-throughput first principles electronic structures to study the metal and the H sub-lattices respectively, and will combine the two to show how metal lattices help the assembly of H covalent network. Finally, the mechanism will be applied to explore the stability of mixed metal superhydrides of which the structure searches and phase diagram calculations are far more difficult.

The chemical templates. The La atoms in LaH_{10} at 300 GPa correspond to a face-centered cubic (FCC) lattice at 12.4 GPa. Strikingly, its ELF exhibits maxima with considerable values of 0.62 and 0.45 at the centers of octahedral (E^O) and tetrahedral (E^T) sites, suggesting some crystal orbitals have large distributions at these areas (Fig. 2a). As a matter of fact, among the 23 occupied crystal orbitals (CO) at the Γ point, states 17 - 19, 20 (Fig. 2b) and 21 – 23 that are 2.96, 2.38 and 2.33 eV below E_F, show maxima and large contributions at E^O sites, both E^O and E^T sites, and E^T sites, respectively. This feature is also found in high-pressure electrides (HPE), in which some electrons localized in the interstitial voids and play the role of anions.[28,29] However, the charge distribution of FCC La shows no maxima at E^O and E^T sites, therefore it is not an HPE.

While the above ELF and the COs are overlaid on the H lattice, a striking feature of the superhydrides emerges unexpectedly. The H lattice matches excellently with the ELFs (Fig. 2c)

and relative COs (Fig. 2d) of the metal lattices that include no information of H atoms at all. The H_{10} lattice in LaH_{10} consists of two types of H, H^1 that forms H_8 cubes locating at the E^O sites, and H^2 locating at E^T sites. Furthermore, some COs of the H_{10} lattice also consist of orbitals locating at E^O and E^T sites. At Γ point, the lowest unoccupied CO 21 (Fig. 2e) consists of orbitals locating at both E^O and E^T. Therefore, while the La and the H_{10} lattices are interposed together, the occupation of E^O and E^T orbitals in La valence bands will naturally dope H_{10} by occupying its conduction bands. Indeed, the highest occupied state 40 of LaH_{10} at the Γ point consists of orbitals at E^O and E^T (Fig. 2f). Therefore, instead of direct charge transfer from La atoms to H atoms, large part of the electron density of La lattice already localizes around the consisting motifs of H lattices, forming a chemical template awaiting and assisting the assembly of the H lattice.

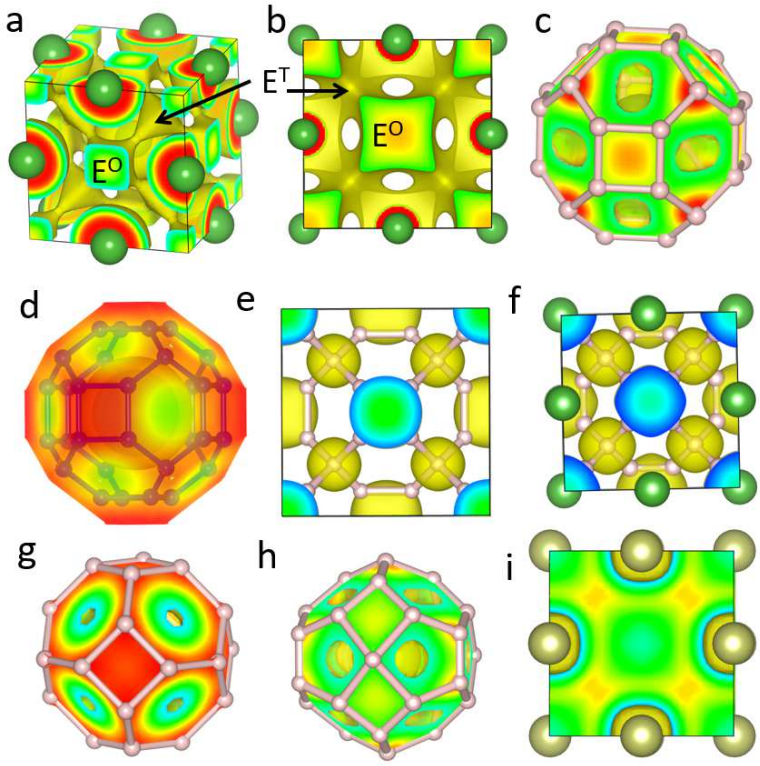

Fig. 2 | The chemical templates in superhydrides. a, The ELF of La lattice (after removing all H atoms) in LaH_{10} superhydrides at 300 GPa. **b**, The density distribution of state number 20 at Γ

point of La lattice in LaH_{10} at 300 GPa. **c**, The same ELF of La lattice overlaid on H_{10} lattice. **d**, The density distribution of state number 17 at Γ point of La lattice in LaH_{10} at 300 GPa, overlaid on the H_{10} lattice. **e**, The density distribution of state number 21 (LUMO) at Γ point of the H_{10} lattice (after removing La atoms) in LaH_{10} at 300 GPa. **f**, The density distribution of state number 40 (HOMO) of LaH_{10} at Γ point at 300 GPa. **g**, The ELF of Sc lattice in ScH_6 at 300 GPa, overlaid on the H_6 lattice. **h**, The ELF of Ce lattice in CeH_9 at 300 GPa, overlaid on the H_9 lattice. **i**, The ELF of Ir lattice in a conceived IrH_{10} with parameters optimized at 300 GPa. The maxima are between the neighboring Ir atoms, instead of at the E^O and E^T interstitial sites.

The close match of the metal ELF and the H lattice is found for all metal superhydrides despite the large variation of structures and symmetries, such as MH_6 in $Im\bar{3}m$ structure (M= Sc, Ca, Y), MH_9 in $P6_3/mmc$ structure (M=Ce, Pr, La, etc.), MH_{10} in $P6_3/mmc$ structure (M=Y, Ac, etc), MH_{12} in $Fm\bar{3}m$ structure (M=Ac, La, Ba) and MH_{16} in P6/mmm structure (M=La, etc.) and many others (Fig. 2g, h and Supplementary Section II). The metals in these superhydrides may adopt many different structures, including FCC, body-center cubic (BCC), hexagonal close-packed (HCP), simple cubic (SC), simple hexagonal (SH), or structures that deformed along high symmetry directions of them. These sub-lattices are not necessary the stable structures of metals. Especially, for non-cubic superhydrides, the stresses of the metal lattices are usually not hydrostatic (Supplementary Table 2). For example, the normal stresses of the Ce lattice in CeH_9 at 300 GPa are $\sigma_1=\sigma_2=1.1$ GPa, $\sigma_3=15.1$ GPa. Nevertheless, all metal lattices show large electron distributions in the interstitial regions that match nicely with the locations and patterns of the H lattices in superhydrides, even if many superhydrides are in low symmetry structures, such as $R\bar{3}m$ SrH_6 and Immm Ti_2H_{13} and the corresponding ELF and H lattices exhibit complicated geometry features. On the other hand, the strength of the template effect that can be estimated by the ELF values at the interstitial sites strongly depends on metals. While they are the strongest for metals at the s-d boarder, they decline quickly for metals away from that region and become insignificant for late transition metals (Supplementary Fig. 2). For example, in an FCC Ir lattice

of a conceived IrH_{10} compounds, the maxima of ELF are no longer at the interstitial sites but in the regions between neighboring Ir atoms (Fig. 2i).

The building units of H lattices. The second key feature of superhydrides is that the H lattices consist of unique and intrinsic building units (Fig. 3a) that are positioned right at the active regions of the metal templates. They can be identified by the geometry, symmetry and the crystal orbitals of H lattices (Fig. 3b, c). Some units are straightforward to identify by their appearance in the lattice, such as H_6 hexagons and H_4 squares in MH_6, and H_8 cubes and H_5 tetrahedrons in MH_{10}; whereas some others are quite unexpected. For example, the H units in MH_9 are not H_5 and H_6 rings, but rather a H_6 corona and a H_8 bipyramid (Fig. 3a). These two units share most of the symmetries of MH_9, and many occupied crystal states localize on them (Fig. 3c). The particular ways that H lattices are divided into building units are also corroborated by their energies that are calculated by use of a He-matrix model (see Methods). Among the 6 building units in MH_6, MH_9 and MH_{10}, the H_6 hexagon, the H_8 cube and the H_6 corona are significantly lower in energy. Also, their energies decrease for about 0.5 eV/atom while pressure increases from 100 GPa to 300 GPa (Fig. 3d).

The remarkable stability of H_6 hexagon, H_8 cube and H_6 corona originates from an important feature of H-H bond. Due to the quantum resonance, these bonds are conjugated and delocalized in the same way as the C-C 2p π bonds in organic molecules of which the stability is controlled by the aromaticity.[30,31] Because of the topology of the π bonds, the aromatic molecules need to assume a planar geometry and their electron counting needs to satisfy 4n+2 rule, which ensures a gap between the fully occupied and unoccupied orbitals. However, in contrast to C π bonds, the

conjugation of H-H bonds is not constrained inside the same plane. The corresponding three-dimensional aromaticity depends on the symmetry and the number of H in the cluster, and the above three H clusters are all aromatic. The energy levels of H_6 hexagon resemble the energy levels of the benzene ring,[30] and the highest occupied (HOMO) and the lowest unoccupied molecular orbitals (LUMO) are doubly degenerate (Fig. 3e). In contrast, the HOMO and LUMO of H_8 cube are triply degenerate (Fig. 3f). The HOMO-LUMO gaps of H_6 hexagon, H_8 cube and H_6 corona are 8.50, 10.15 and 7.77 eV, respectively. Many other aromatic H clusters are also identified as building units in various superhydrides (Supplementary Section V).

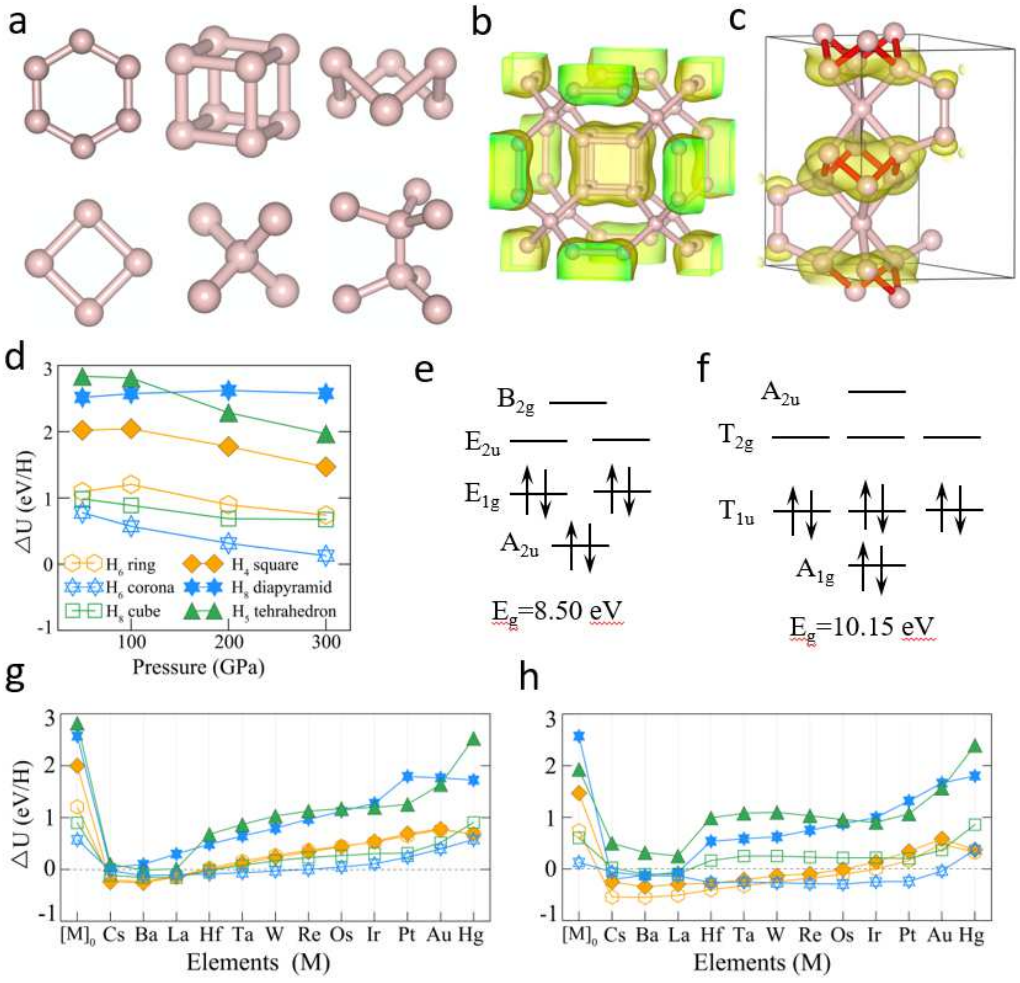

Fig. 3 | The assembly of the H lattices on metal templates. a, The six building units of the H lattices in MH_6, MH_{10} and MH_9 superhydrides, including the H_6 hexagon, the H_4 square, the H_8

cube, the H_5 tetrahedron, the H_6 corona and the H_8 bipyramid. **b**, The density distribution of state number 2 at Γ point of H_{10} lattice (after removing La atoms) in LaH_{10} at 300 GPa, showing the localization of the crystal orbital on H_8 cubes. **c**, The density distribution of state number 2 at Γ point of H_9 lattice (after removing Ce atoms) in CeH_9 at 300 GPa, showing the localization of the crystal orbital on H_6 coronas. In order to illustrate H_6 coronas, their H-H bonds are shown in red. **d**, The energies of the H units relative to H_2 molecules as functions of pressure. The calculations are performed by use of the He matrix model. **e**, The symmetries and the calculated energy levels of a H_6 hexagon. **f**, The symmetries and the calculated energy levels of a H_8 cube. **g**, The energies of the H units relative to H_2 with the presence of metals in the 6th row of periodic table, calculated by use of the He matrix at 100 GPa. **h**, The energies of the H units relative to H_2 with the presence of metals in the 6th row of periodic table, calculated by use of the He matrix at 300 GPa.

The assembly of H covalent network on metal templates. In this section, we will demonstrate that the presence of the metal sub-lattices greatly improve the stability of H building units. This is due to the presence of the chemical template effects in metal lattices (Supplementary Fig. 3), and the strength of this effect is determined by ELF intensities that strongly depend on the metal as well as the pressure. We employ high throughput calculations using the He matrix model that allows comparing energies of H clusters with H_2 molecules in the same chemical environment (see Methods). The results show that the presence of the metal atoms can lower the energies of H units relative to H_2 for about 0.5 to 3 eV, including non-aromatic ones such as H_4 squares and H_5 tetrahedrons (Fig. 3g, h and Supplementary Fig. 4). This template effect strongly depends on metals. The most profound changes happen to the elements around the s-d border and decline with increasing number of d electrons, which is consistent with the trend of ELF (Supplementary Fig. 2). Among row 6 elements, those sit at the s-d border such as Ba and La can lower the energies of all H units except H_5 below H_2 at 300 GPa; whereas late transition metals such as Pt and Au show much weaker effect. Very few elements, including Ba, La and Th etc, could bring the energy of H_8 cube below H_2.

Pressure is essential to the stability of H lattice, by virtue of directly lowering the energies of H units and influencing the effect of metal templates. The distances between metal atoms are larger under lower pressure, reducing the electron density in the interstitial region and weakening the chemical driving force from the templates. The expansion of the metal lattices and the reduction of the template effect will also happen while more H atoms are packed into them, therefore placing limits to H compositions of superhydrides.

The concept of chemical template provides a very different view to chemical bonds in solid compounds. The strong chemical interactions due to the template effect do not associate with large electron relocations in contrast to both ionic and covalent bonds. The electron distributions in superhydrides are optimal not only to the whole compound but also to its consisting metal and H sub-lattices, which maximize the stability. Taking LaH_{10} as an example, the summation of the density distributions of the sub-lattices $\rho(La+H_{10}) = \rho[La\ lattice] + \rho[H_{10}]$ resemble very nicely $\rho(LaH_{10})$ (Supplementary Fig. 5a), which can be seen more clearly by the fact that $\Delta\rho = \rho(LaH_{10}) - \rho(La+H_{10})$ is quite small. As a matter of fact, the integrated transferred charge calculated from $\Delta\rho$ is about -0.15e for La (Supplementary Fig. 5b), which is about 10 times smaller than the Bader charge calculated from $\rho(LaH_{10})$ (Supplementary Fig. 5c). The negative value indicates an electron transfer to La, which can be misinterpreted as the presence of anionic La,[32] while it is actually the transfer of a small portion of charges around E^O and E^T back to La.

Chemical templates in mixed-metal superhydrides. The chemical template theory illuminates the search of novel superhydrides in a wider composition space including the ternary and quaternary compounds,[33–36] which is important for achieving room-temperature

superconductivity at lower pressure. Constructing a complete phase diagram of ternary superhydrides based on full-scale DFT calculations is extremely difficult, and the search of optimal compounds across the entire periodic table as we have done for binary superhydrides is an impossible task. To date, only Li-Mg-H ternary phase diagram has been thoroughly searched, which predicted a metastable superhydride, Li_2MgH_{16}, that shows a T_c of ~473K at 250 GPa.[37] In contrast, the template theory allows us to assess the formation of mixed-metal superhydrides by studying only the metal lattices. High-throughput calculations show strong correlation between the enhancements of the template strength while mixing metals and the energy of formation of mixed metal superhydrides.

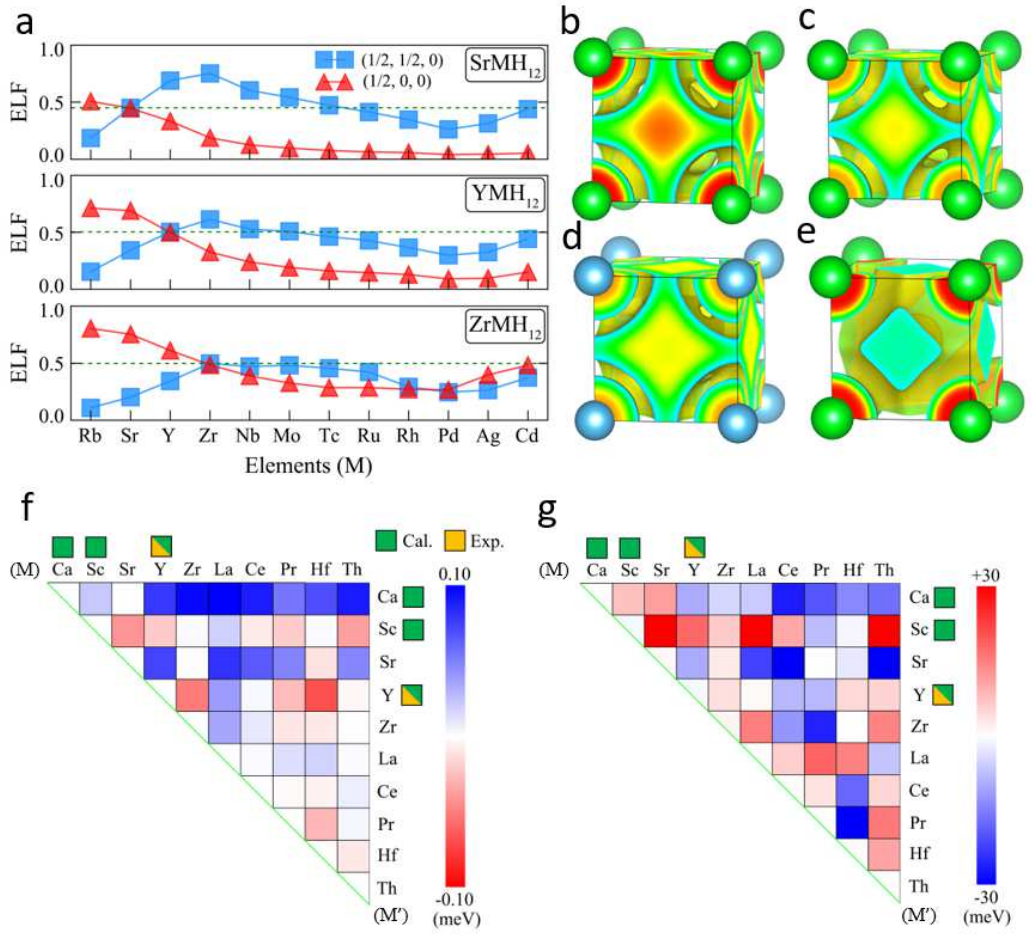

Fig. 4 | The chemical template effects in mixed-metal superhydrides. a, The ELF values of $MM'H_{12}$ mixed metal superhydrides at the interstitial points, including (1/2, 1/2, 0) and (1/2, 0,

0). M is Sr, Y and Zr, and M′ is a 5th row metal element. **b-e**, The ELF of $SrYH_{12}$, $SrZrH_{12}$, $YZrH_{12}$ and $SrAgH_{12}$. **f**, The average ELF of $MM'H_{12}$ superhydrides at 100 GPa, $\Delta ELF = ELF^{1/2,1/2,0}_{MM'H_{12}} + ELF^{1/2,0,0}_{MM'H_{12}} - ELF_{MH_6} - ELF_{M'H_6}$, in which M and M′ are Ca, Sc, Sr, Y, Zr, La, Ce, Pr, Hf and Th. **g**, The reaction enthalpy of forming $MM'H_{12}$, $\Delta H = (H(MM'H_{12}) - H(MH_6) - H(M'H_6))/14$, at 100 GPa. In both (**f**) and (**g**) the squats filled with green and orange colors show MH_6 superhydrides that are predicted by DFT calculations and synthesized by DAC experiments, respectively.

The ELF is calculated for two-metal lattices adapted from metal structures in MH_6, MH_{10}, and MH_9 at 100 GPa by partially replacing metal atoms (1 in a conventional cell) with other metals (Fig. 4a-e and Supplementary Fig. 6). The results clearly show the mixture with later transition metals greatly lowers the ELF values at the interstitial sites, therefore reduces the strength of the template effect. As a matter of fact, the ELF shows maxima at the interstitial sites only while mixing with metals close to s-d boarder such as Sr, Y and Zr (Fig. 4b-d), but not with late transition metals, such as Ag (Fig. 4e). We therefore focus on the combination of template "active" metals. While forming $MM'H_{12}$ superhydrides by mixing MH_6 and $M'H_6$, the change of the template strength is measured by $\Delta ELF = ELF^{1/2,1/2,0}_{MM'H_{12}} + ELF^{1/2,0,0}_{MM'H_{12}} - ELF_{MH_6} - ELF_{M'H_6}$, whereas the stability of the mixed superhydrides is measured by reaction enthalpies $\Delta H = [H(MM'H_{12}) - H(MH_6) - H(M'H_6)]/14$, for $MM'H_{12}$. The comparison of the two reveals a strong correlation, namely the enhancement of ELF in a mixed metal lattice often corresponds to a stable mixed metal superhydride (Fig. 4f, g). For example, while mixing Sr and Y, the average ELF increases (Fig. 4b) and the $SrYH_{12}$ is stable against the decomposition into SrH_6 and YH_6 (Fig. 4g). In contrast, the mixture of Y and Zr leads to lower average ELF (Fig. 4c) and correspondingly $YZrH_{12}$ is not stable (Fig. 4g). As expected, the stability shows stronger correlation with ELF while the change of ELF is more significant, because stability is also affected by many other factors such as the strain energy caused by the different sizes of two

metals. Furthermore, the stability of mixed-metal superhydrides also depends on structure (Supplementary Fig. 7). The sodalite MH_6 seems hard to mix, whereas forming $MM'H_{18}$ is often exothermic. Even if a metal superhydride is not stable, it might still be stabilized by forming mixed metal superhydrides, if the enthalpy of the metastable MH_n is not much off the convex hull. Therefore, a large-scale study of the mixed metal lattices adapted from known intermetallic compounds and the change of their ELF is a promising and affordable approach to predicting mixed metal superhydrides. The mixed metal lattices adapted from MH_6, MH_{10} and MH_9 in this work are also structures of known intermetallic compounds; and the Li-Mg lattice in Li_2MgH_{16} is isostructural to Laves phase $MgCu_{12}$.[37]

Conclusions

By studying the mechanism of metal superhydrides formation, we revealed an unexpected driving force of forming solid compounds, *i.e.* the chemical template effect. Different to the traditional chemical bond theory that compares the compounds with free atoms, we view the formation of superhydrides as the interposition of metal and H sub-lattices. Our calculations showed large electron distributions at the interstitial sites due to the occupation of the crystal orbitals of the metal sublattices, forming chemical templates. They assist the dissociation of H_2 molecules and the formation of H covalent networks in superhydrides. Furthermore, the H sublattices consist of H building units that are aromatic despite that they are not planar. Calculations using He-matrices show that the presence of the metal sub-lattices can largely stabilize the building units of the H lattices. The chemical template mechanism can also be applied to help the exploration of ternary (mixed metal) superhydrides. High-throughput calculations revealed a strong correlation between the strength of the chemical templates and the stability of the mixed metal superhydrides, indicating it can be used for a large-scale search of

ternary and quaternary superhydrides. It will greatly enhance the efficiency of searching superhydride materials that might become superconducting at higher temperature and lower pressure.

5

Methods

Solid-state density functional calculations. The underlying first-principles density functional theory (DFT) calculations were carried out by using the plane-wave pseudopotential method as implemented in Vienna *ab initio* Simulation Package (VASP).[38,39] The electron-ion interactions were described by the projector augmented wave pseudopotentials[40,41] and the used valence electrons are listed in Table 1. We used the generalized gradient approximation formulated by Perdew, Burke, and Ernzerhof[42] as exchange-correlation functional. A kinetic energy cutoff of 520 eV was adopted for wave-function expansion. The *k*-point meshes with interval smaller than $2\pi \times 0.03$ Å^{-1} for electronic Brillouin zone to ensure that all enthalpy calculations converged within 0.02 eV/atom.

H											He
$1s^1$											$1s^2$
K	Ca	Sc	Ti	V	Cr	Mn	Fe	Co	Ni	Cu	Zn
$3s^23p^64s^1$	$3p^64s^2$	$3d^14s^2$	$3d^24s^2$	$3d^34s^2$	$3d^54s^1$	$3d^54s^2$	$3d^64s^2$	$3d^74s^2$	$3d^84s^2$	$3d^{10}4s^1$	$3d^{10}4s^2$
Rb	Sr	Y	Zr	Nb	Mo	Tc	Ru	Rh	Pd	Ag	Cd
$4s^24p^65s^1$	$4s^24p^65s^2$	$4s^24p^64d^15s^2$	$4d^25s^2$	$4s^24p^64d^35s^2$	$4d^55s^1$	$4d^55s^2$	$4d^65s^2$	$4d^75s^2$	$4d^85s^2$	$4d^{10}5s^1$	$4d^{10}5s^2$
Cs	Ba	La	Hf	Ta	W	Re	Os	Ir	Pt	Au	Hg
$5s^25p^66s^1$	$5s^25p^66s^2$	$5s^25p^65d^16s^2$	$5d^26s^2$	$5d^36s^2$	$5d^56s^1$	$5d^56s^2$	$5d^66s^2$	$5d^76s^2$	$5d^86s^2$	$5d^{10}6s^1$	$5d^{10}6s^2$
		Ce	Pr	Ac	Th	Pa	U				
		$5s^25p^64f5d6s^2$	$5s^25p^64f^36s^2$	$6s^26p^66d7s^2$	$6s^26p^66d^27s^2$	$6s^26p^65f^26d7s^2$	$6s^26p^65f^36d7s^2$				

Table 1. The valence configurations of the pseudopotentials used in our solid-state DFT calculations.

Energy analysis of H in superhydrides. In order to compare the energy terms, including the enthalpies, the internal energies and the PV terms, of the hydrogen in superhydrides directly with pristine hydrogen phases under pressure, we deduct the corresponding energies of the metal hydrides with typical composition, and refer it to those of C_2/c molecular H_2 phase. For example,

the enthalpy H of the H incorporated into LaH_{10} beyond its typical composition LaH_3 is calculated as $\Delta H(\mathrm{H}) = [H(\mathrm{LaH_{10}}) - H(\mathrm{LaH_3}) - \frac{7}{2} \times \mathrm{H}(\mathrm{H_2}^{C2/c})]/7$. Similar formula is used to calculate $\Delta U(\mathrm{H})$ and $\Delta PV(\mathrm{H})$. These energy terms are used to compare with the corresponding values of pristine H phases, as shown in Fig. 1d-f and Supplementary Fig. 1.

Electronic structure Analyses of solid compounds. The electronic structures of metal superhydrides are calculated and analyzed by use of several methods, including the Bader's Quantum Theory of Atoms in Molecules (QTAIM),[43] the Electron Localization Function (ELF),[26] the Crystalline Orbital Hamiltonian Population (COHP) and integrated COHP (ICOHP),[25] and integrated differential charge density (see below), etc.

Integrated differential electron density. First, for a given metal superhydride (MH_n), three electron densities are calculated, including that of MH_n, of the metal lattice (MH_n after removing all H), and of the H lattice (MH_n after removing all metals). The differential electron density is then calculated as $\Delta\rho = \rho(MH_n) - \rho[\text{metal lattice}] - \rho[H_n \text{ lattice}]$. This differential density distribution is separated into regions by the surface(s) of $\Delta\rho=0$. Especially, all the metal atoms are surrounded by a surface of $\Delta\rho=0$ that is roughly spherical. In all the cases, $\Delta\rho>0$ inside the surface, indicating that electrons transfer toward metal atoms while interposing the metal and the H lattices. The total charge transfers to metals are calculated by integrating the differential electron density inside the $\Delta\rho=0$ surface. The charges shown in Supplementary Fig. 5c are negative because the electron charge is negative.

Quantum chemistry calculations on H clusters. The geometry parameters of all H clusters are

adapted from the superhydrides optimized by solid-state DFT calculations at the studied pressures (100 and 300 GPa). Their molecular orbitals and the energy levels are calculated by using Gaussian 09 package.[44] The restricted open-shell B3LYP[45–47] and Hartree-Fock[48] methods are used for exchange and correlation functional for H cluster with even and odd number of H atoms respectively, respectively. The 6-31G(d) basis set is adopted for all the single-point calculations.

He matrix model. We build He matrix models to study the energies of various H clusters that are the building units of H lattices in superhydrides and compare them with H_2 molecules in the same chemical environment. Taking LaH_{10} as an example, we first optimize its structure to a selected pressure, for example 300 GPa. A supercell is constructed by triple the units in all three directions. After that, we replace all the H atoms with He atoms. By keeping or removing La metal atoms, we constructed two models, He_{320} and $La_{32}He_{320}$. The H clusters are created in these models by replacing corresponding He atoms with H atoms. For example, while modeling H_8 cubes, we replace 8 He atoms in a cube with H atoms. For comparison with H_2 molecules, we replace four pairs of He atoms in H_{320} and $La_{32}He_{320}$ by four pairs of H atoms. In order to compare the energies of H cluster with H_2 molecules at the same chemical environment, each H_2 molecule is placed at the sites that are part of H cluster. Also, the H_2 molecules are positioned to maximize their distances so to minimize the factitious H_2-H_2 interactions in the model. The H coordinates in H_2 models are relaxed in order to maintain the lowest energy of H_2 molecules inside the He matrix. The relaxed H-H bond lengths in these models are close to that of H_2 molecules at ambient condition. The H atoms in the models of H clusters are not relaxed so that the H-H distances in these clusters are kept the same as in the H lattice of LaH_{10} at the studied

pressure. Similarly, the supercell He-matrix models, including He_{96} and $Y_{16}H_{96}$, are constructed for YH_6, and the energies of H_4 square and H_6 hexagon are studied using these models. The supercell He-matrix models, including He_{144} and $Ce_{16}He_{144}$, are constructed for CeH_9, and the energies of H_6 corona and H_8 bipyramid are studied using them. In high-throughput calculations, metals in superhydrides vary, and the corresponding He-matrix model are created from the MH_n lattice optimized at the studied pressure.

Stability of mixed-metal superhydrides. The stability of the mixed-metal superhydrides is assessed by comparing their enthalpies with their constituent binary superhydrides. The enthalpy differences per atoms as shown in Supplementary Fig. 7 are calculated by the following formulae for three types of superhydrides based on $Im\bar{3}m$ MH_6, $P6_3/mmc$ MH_9 and $Fm\bar{3}m$ MH_{10} superhydride structures. Specifically, the enthalpy differences are defined as:

$\Delta H = (H(\mathrm{MM'H_{12}}) - H(\mathrm{MH_6}) - H(\mathrm{M'H_6}))/14$, for $\mathrm{MM'H_{12}}$;

$\Delta H = (H(\mathrm{MM'H_{18}}) - H(\mathrm{MH_9}) - H(\mathrm{M'H_9}))/20$, for $\mathrm{MM'H_{18}}$;

$\Delta H = (H(\mathrm{M_nM'_mH_{40}}) - \frac{n}{4}\times H(\mathrm{M_4H_{40}}) - \frac{m}{4}\times(H(\mathrm{M'_4H_{40}}))/44$, for $\mathrm{M_1M'_3H_{40}}$, and $\mathrm{M_3M'_1H_{40}}$, where $H(\mathrm{MM'H_{12}})$, $H(\mathrm{MH_6})$, $H(\mathrm{M'H_6})$, $H(\mathrm{MM'H_{18}})$, $H(\mathrm{MH_9})$, $H(\mathrm{M'H_9})$, $H(\mathrm{M_nM'_mH_{40}})$, $H(\mathrm{M_4H_{40}})$, and $H(\mathrm{M'_4H_{40}})$ represents the enthalpies of ternary and binary superdydrides. Their structures are optimized at 100 and 300 GPa. M and M′ represents the metals in 1-12 groups of 4-6 periods.

Data availability

The authors declare that all of the data supporting the findings of this study are available within the paper and the Supplementary Information, and also from the corresponding authors upon reasonable request.

References

1. Ashcroft, N. W. Metallic Hydrogen: A High-Temperature Superconductor? *Phys. Rev. Lett.* **21**, 1748–1749 (1968).
2. Ashcroft, N. W. Hydrogen Dominant Metallic Alloys: High Temperature Superconductors? *Phys. Rev. Lett.* **92**, 187002 (2004).
3. R. J., H., M., A., H., L. & M., S. *in Proceedings of the International Symposium - Superconductivity and Pressure: A Fruitful Relationship on the Road to Room Temperature Superconductivity*. (in Proceedings of the International Symposium - Superconductivity and Pressure: A Fruitful Relationship on the Road to Room Temperature Superconductivity(ed. Alario-Franco, M. A.) 199–213 (Fundación Ramón Areces, 2019).).
4. Mao, H. & Hemley, R. J. Ultrahigh-pressure transitions in solid hydrogen. *Rev. Mod. Phys.* **66**, 671–692 (1994).
5. Gregoryanz, E. *et al.* Everything you always wanted to know about metallic hydrogen but were afraid to ask. *Matter and Radiation at Extremes* **5**, 038101 (2020).
6. Errea, I. *et al.* Quantum hydrogen-bond symmetrization in the superconducting hydrogen sulfide system. *Nature* **532**, 81–84 (2016).
7. Snider, E. *et al.* Room-temperature superconductivity in a carbonaceous sulfur hydride. *Nature* **586**, 373–377 (2020).
8. Miao, M., Sun, Y., Zurek, E. & Lin, H. Chemistry under high pressure. *Nature Reviews Chemistry* 1–20 (2020) doi:10.1038/s41570-020-0213-0.
9. Peng, F. *et al.* Hydrogen Clathrate Structures in Rare Earth Hydrides at High Pressures: Possible Route to Room-Temperature Superconductivity. *Phys. Rev. Lett.* **119**, 107001 (2017).

10. Liang, X. *et al.* Potential high-Tc superconductivity in CaYH12 under pressure. *Phys. Rev. B* **99**, 100505 (2019).

11. Li, X. *et al.* Polyhydride CeH 9 with an atomic-like hydrogen clathrate structure. *Nature Communications* **10**, 3461 (2019).

12. Wang, H., Tse, J. S., Tanaka, K., Iitaka, T. & Ma, Y. Superconductive sodalite-like clathrate calcium hydride at high pressures. *PNAS* **109**, 6463–6466 (2012).

13. Ye, X., Zarifi, N., Zurek, E., Hoffmann, R. & Ashcroft, N. W. High Hydrides of Scandium under Pressure: Potential Superconductors. *J. Phys. Chem. C* **122**, 6298–6309 (2018).

14. Semenok, D. V. *et al.* Superconductivity at 161 K in thorium hydride ThH10: Synthesis and properties. *Materials Today* **33**, 36–44 (2020).

15. Kruglov, I. A. *et al.* Uranium polyhydrides at moderate pressures: Prediction, synthesis, and expected superconductivity. *Science Advances* **4**, eaat9776 (2018).

16. Zhou, D. *et al.* Superconducting praseodymium superhydrides. *Science Advances* **6**, eaax6849 (2020).

17. Flores-Livas, J. A., Sanna, A. & Gross, E. K. U. High temperature superconductivity in sulfur and selenium hydrides at high pressure. *Eur. Phys. J. B* **89**, 63 (2016).

18. Pickard, C. J., Errea, I. & Eremets, M. I. Superconducting Hydrides Under Pressure. *Annu. Rev. Condens. Matter Phys.* **11**, 57–76 (2020).

19. Errea, I. *et al.* Quantum crystal structure in the 250-kelvin superconducting lanthanum hydride. *Nature* **578**, 66–69 (2020).

20. Zurek, E. & Bi, T. High-temperature superconductivity in alkaline and rare earth polyhydrides at high pressure: A theoretical perspective. *J. Chem. Phys.* **150**, 050901 (2019).

21. Azadi, S., Monserrat, B., Foulkes, W. M. C. & Needs, R. J. Dissociation of High-Pressure Solid Molecular Hydrogen: A Quantum Monte Carlo and Anharmonic Vibrational Study. *Phys. Rev. Lett.* **112**, 165501 (2014).

22. McMahon, J. M. & Ceperley, D. M. Ground-State Structures of Atomic Metallic Hydrogen. *Phys. Rev. Lett.* **106**, 165302 (2011).

23. Goncharov, A. Phase diagram of hydrogen at extreme pressures and temperatures; updated through 2019 (Review article). *Low Temperature Physics* **46**, 97–103 (2020).

24. Howie, R. T., Guillaume, C. L., Scheler, T., Goncharov, A. F. & Gregoryanz, E. Mixed Molecular and Atomic Phase of Dense Hydrogen. *Phys. Rev. Lett.* **108**, 125501 (2012).

25. Dronskowski, R. & Bloechl, P. E. Crystal orbital Hamilton populations (COHP): energy-resolved visualization of chemical bonding in solids based on density-functional calculations. *J. Phys. Chem.* **97**, 8617–8624 (1993).

26. Silvi, B. & Savin, A. Classification of chemical bonds based on topological analysis of electron localization functions. *Nature* **371**, 683–686 (1994).

27. Pauling, L. *The Nature of the Chemical Bond*. (Cornell University Press, 1960).

28. Miao, M.-S. & Hoffmann, R. High Pressure Electrides: A Predictive Chemical and Physical Theory. *Acc. Chem. Res.* **47**, 1311–1317 (2014).

29. Miao, M. & Hoffmann, R. High-Pressure Electrides: The Chemical Nature of Interstitial Quasiatoms. *J. Am. Chem. Soc.* **137**, 3631–3637 (2015).

30. Naumov, I. I. & Hemley, R. J. Aromaticity, Closed-Shell Effects, and Metallization of Hydrogen. *Acc. Chem. Res.* **47**, 3551–3559 (2014).

31. Carey, F. A. & Sundberg, R. J. *Advanced Organic Chemistry, Part A: Structure and Mechanisms*. (Springer, 2008).

32. Liu, L. *et al.* Microscopic mechanism of room-temperature superconductivity in compressed LaH10. *Phys. Rev. B* **99**, 140501 (2019).

33. Liu, H., Naumov, I. I., Hoffmann, R., Ashcroft, N. W. & Hemley, R. J. Potential high-Tc superconducting lanthanum and yttrium hydrides at high pressure. *Proceedings of the National Academy of Sciences* **114**, 6990 (2017).

34. Chen, J. *et al.* Computational Design of Novel Hydrogen-Rich YS–H Compounds. *ACS Omega* **4**, 14317–14323 (2019).

35. Shao, Z. *et al.* Ternary superconducting cophosphorus hydrides stabilized via lithium. *npj Computational Materials* **5**, 1–8 (2019).

36. Cui, W. *et al.* Route to high-Tc superconductivity via CH4-intercalated H3S hydride perovskites. *Phys. Rev. B* **101**, 134504 (2020).

37. Sun, Y., Lv, J., Xie, Y., Liu, H. & Ma, Y. Route to a Superconducting Phase above Room Temperature in Electron-Doped Hydride Compounds under High Pressure. *Phys. Rev. Lett.* **123**, 097001 (2019).

38. Kresse, G. & Furthmüller, J. Efficiency of ab-initio total energy calculations for metals and semiconductors using a plane-wave basis set. *Comput. Mater. Sci.* **6**, 15–50 (1996).

39. Kresse, G. & Furthmüller, J. Efficient iterative schemes for ab initio total-energy calculations using a plane-wave basis set. *Phys. Rev. B* **54**, 11169–11186 (1996).

40. Kresse, G. & Joubert, D. From ultrasoft pseudopotentials to the projector augmented-wave method. *Phys. Rev. B* **59**, 1758–1775 (1999).

41. Blöchl, P. E. Projector augmented-wave method. *Phys. Rev. B* **50**, 17953–17979 (1994).

42. Perdew, J. P., Burke, K. & Ernzerhof, M. Generalized gradient approximation made simple. *Phys. Rev. Lett.* **77**, 3865–3868 (1996).

43. Bader, R. F. W. *Atoms in Molecules: A Quantum Theory*. (Clarendon Press, 1994).

44. Frisch, M. J. *et al. Gaussian 16 Rev. C.01*. (2016).

45. Becke, A. D. Density□functional thermochemistry. III. The role of exact exchange. *J. Chem. Phys.* **98**, 5648–5652 (1993).

46. Lee, C., Yang, W. & Parr, R. G. Development of the Colle-Salvetti correlation-energy formula into a functional of the electron density. *Phys. Rev. B* **37**, 785 (1988).

47. Miehlich, B., Savin, A., Stoll, H. & Preuss, H. Results obtained with the correlation energy density functionals of becke and Lee, Yang and Parr. *Chemical Physics Letters* **157**, 200–206 (1989).

48. Tsuchimochi, T. & Scuseria, G. E. Communication: ROHF theory made simple. *J. Chem. Phys.* **133**, 141102 (2010).

Acknowledgements:

M.M. and Y.S. acknowledge the support of NSF CAREER award 1848141, M.M. also acknowledges the support of ACS PRF 59249-UNI6 and the support of California State University Research, Scholarship and Creative Activity (RSCA) award. We thank the computational resources provided by XSEDE (TG-DMR130005).

Author contributions:

M.M. proposed the chemical template mechanism and designed the research. Y.S. conducted all the calculations. M.M. and Y.S. analyzed the results together. M.M. wrote the manuscript. M.M. and Y.S. plotted the figures together.

Competing interests:

The authors declare no competing interests.

Figures

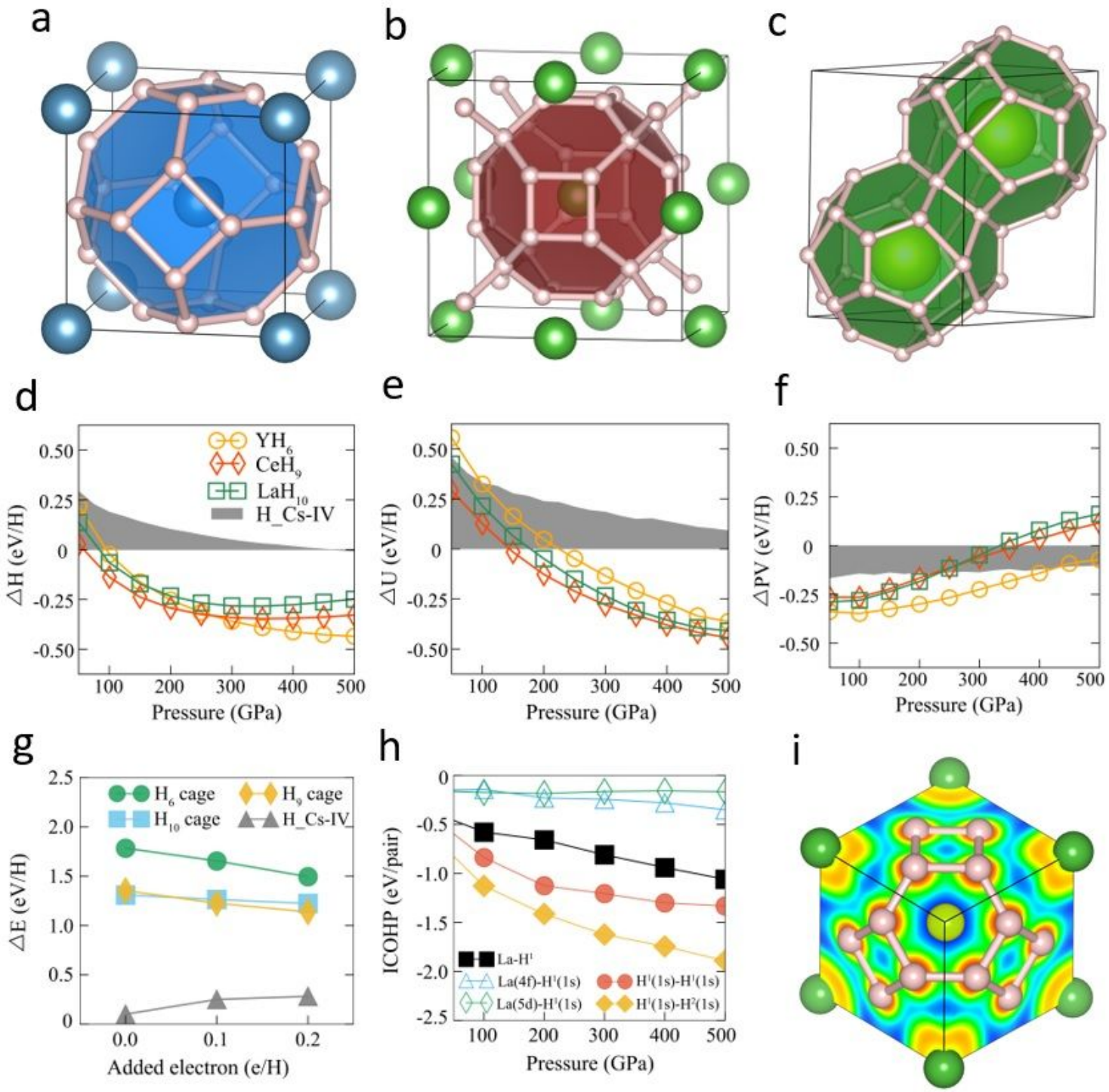

Figure 1

Structure, stability and bonding features of metal superhydrides. a-c, The sodalite structures of three major types of metal superhydrides, including CaH6 in ⍰⍰3⍰ structure, LaH10 in ⍰⍰3⍰ structure, and CeH9 in ⍰6!/⍰⍰⍰ structure. The large blue, green and yellow balls represent the Ca, La, and Ce atoms; and the small white balls represent the H atoms. d-f, The extracted enthalpy (Δ⍰), internal energy (Δ⍰) and ⍰Δ⍰ term of hydrogen in superhydrides relative to pristine hydrogen in molecular phase as functions of

pressure (Method). The shaded areas show Δ, Δ, and Δ of metallic H in Cs-IV structure. g, The internal energies of hydrogen lattices (after removing metal atoms from superhydridies) in CaH6, LaH10, and CeH9 and of metallic hydrogen in Cs-IV structure relative to molecular hydrogen phase as functions of added charges. h, The integrated crystalline orbital Hamiltonian population (ICOHP) of La–H, La 5d – H1 1s, La 4f – H1 1s, H1 – H1, and H1 – H2 as functions of pressure. i, The electron localization function (ELF) of YH6 at 300 GPa, viewed from (111) direction. A [111] cutoff plane is placed at a distance of 4.40 Å from the origin.

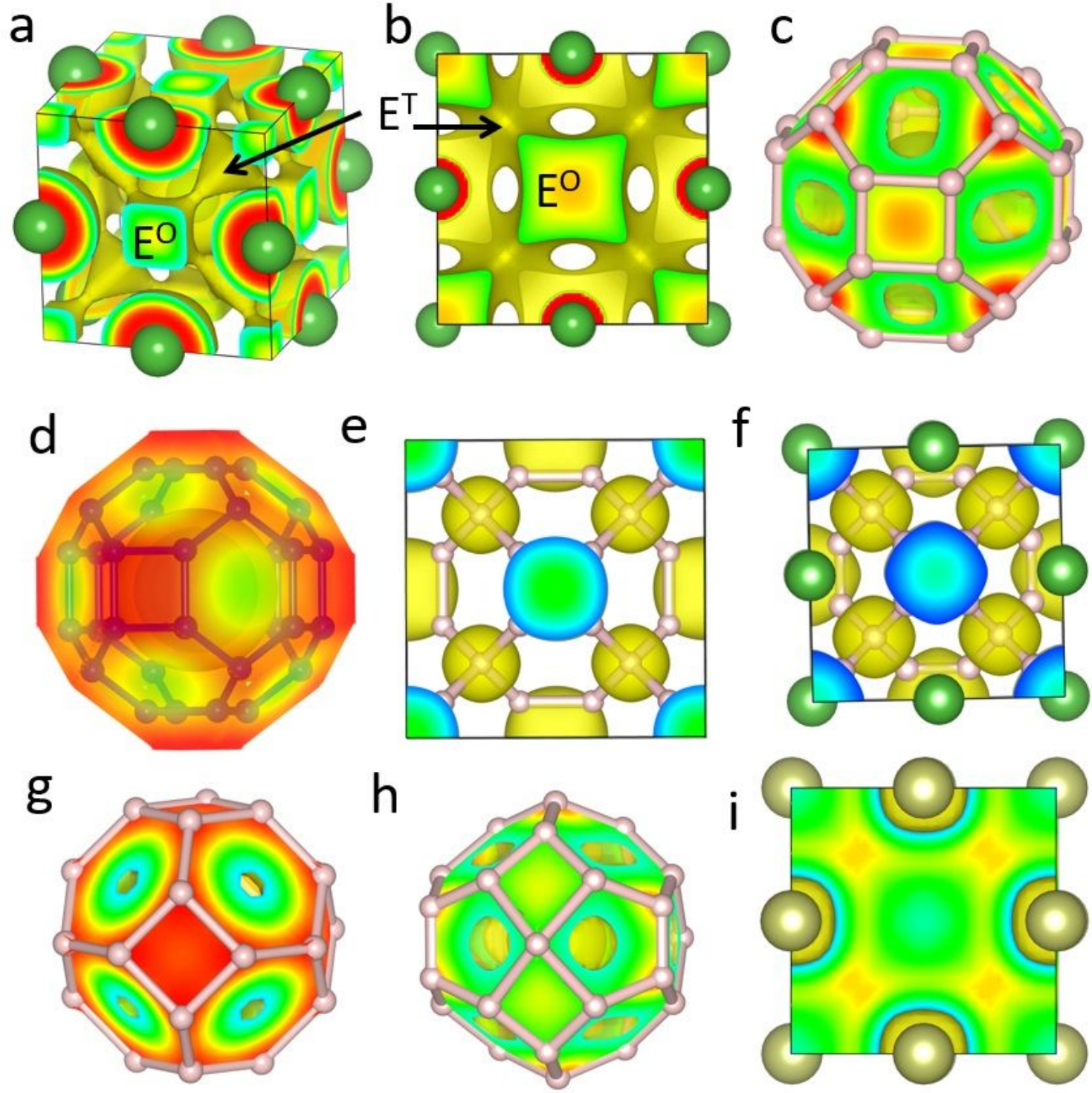

Figure 2

The chemical templates in superhydrides. a, The ELF of La lattice (after removing all H atoms) in LaH10 superhydrides at 300 GPa. b, The density distribution of state number 20 at Γ point of La lattice in LaH10 at 300 GPa. c, The same ELF of La lattice overlaid on H10 lattice. d, The density distribution of state number 17 at Γ point of La lattice in LaH10 at 300 GPa, overlaid on the H10 lattice. e, The density distribution of state number 21 (LUMO) at Γ point of the H10 lattice (after removing La atoms) in LaH10 at 300 GPa. f, The density distribution of state number 40 (HOMO) of LaH10 at Γ point at 300 GPa. g, The ELF of Sc lattice in ScH6 at 300 GPa, overlaid on the H6 lattice. h, The ELF of Ce lattice in CeH9 at 300 GPa, overlaid on the H9 lattice. i, The ELF of Ir lattice in a conceived IrH10 with parameters optimized at 300 GPa. The maxima are between the neighboring Ir atoms, instead of at the EO and ET interstitial sites.

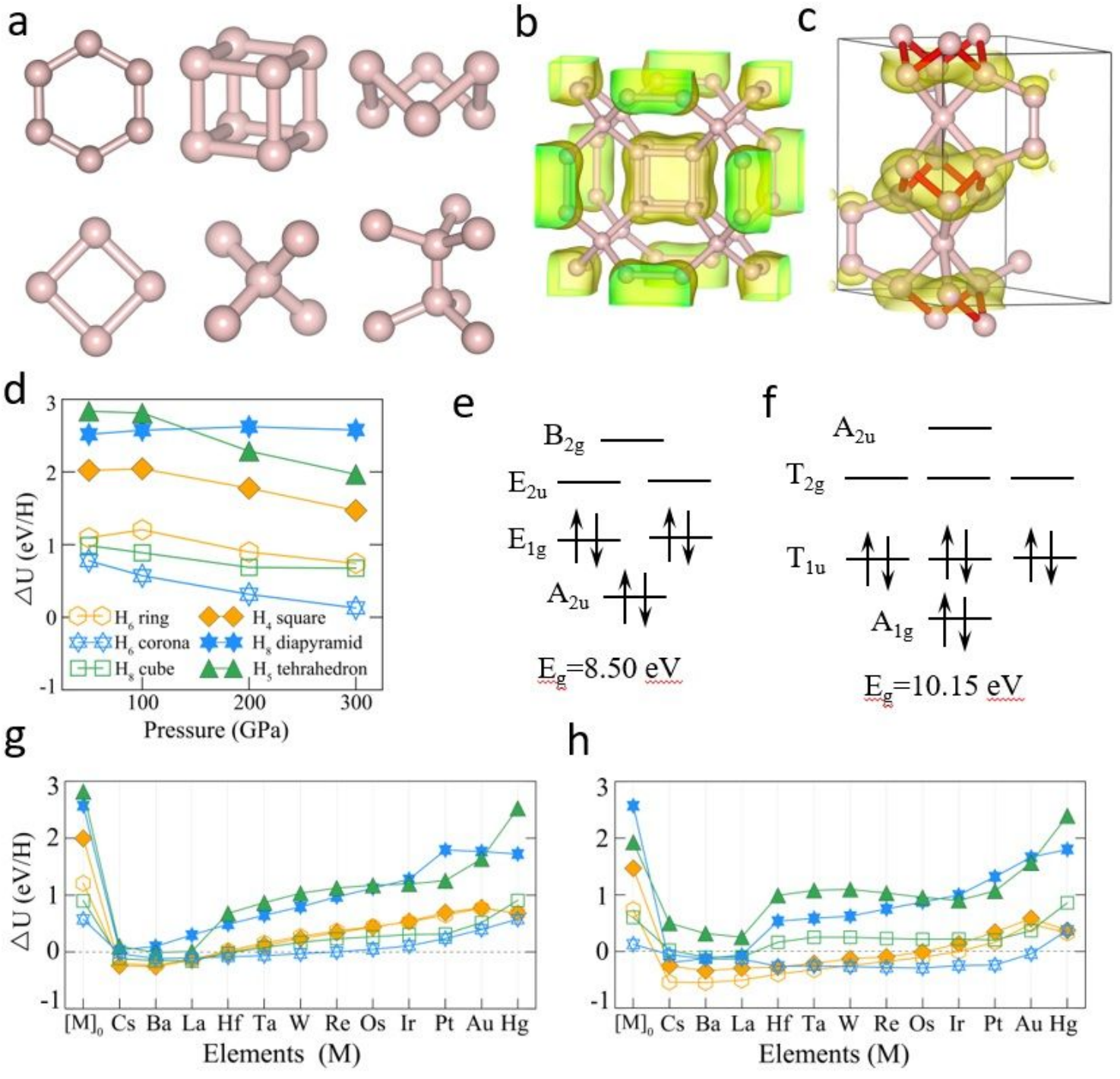

Figure 3

The assembly of the H lattices on metal templates. a, The six building units of the H lattices in MH6, MH10 and MH9 superhydrides, including the H6 hexagon, the H4 square, the H8 cube, the H5 tetrahedron, the H6 corona and the H8 bipyramid. b, The density distribution of state number 2 at Γ point of H10 lattice (after removing La atoms) in LaH10 at 300 GPa, showing the localization of the crystal orbital on H8 cubes. c, The density distribution of state number 2 at Γ point of H9 lattice (after removing Ce atoms) in CeH9 at 300 GPa, showing the localization of the crystal orbital on H6 coronas. In order to illustrate H6 coronas, their H-H bonds are shown in red. d, The energies of the H units relative to H2 molecules as functions of pressure. The calculations are performed by use of the He matrix model. e, The symmetries and the calculated energy levels of a H6 hexagon. f, The symmetries and the calculated energy levels of a H8 cube. g, The energies of the H units relative to H2 with the presence of metals in the 6th row of periodic table, calculated by use of the He matrix at 100 GPa. h, The energies of the H units relative to H2 with the presence of metals in the 6th row of periodic table, calculated by use of the He matrix at 300 GPa.

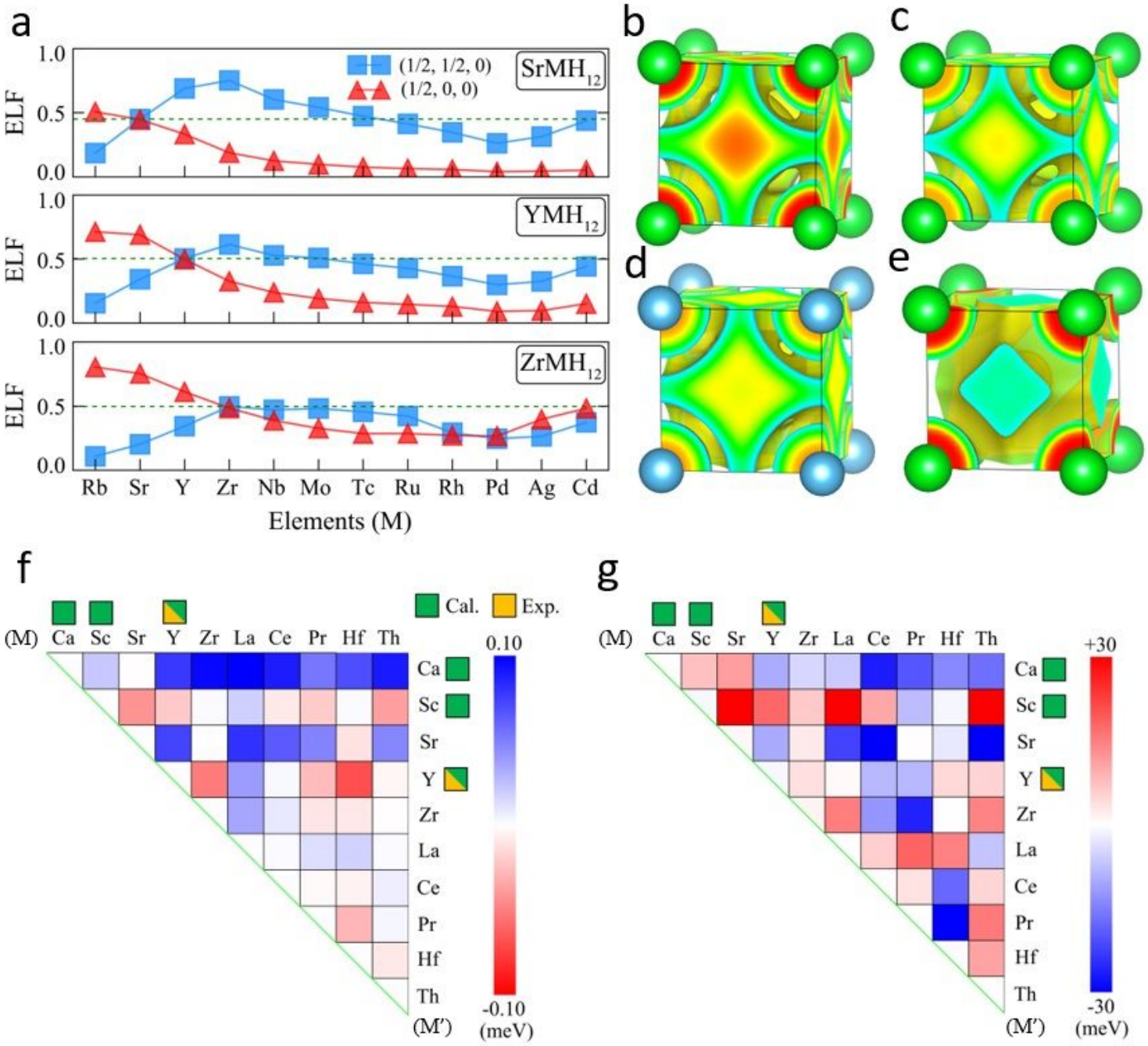

Figure 4

The chemical template effects in mixed-metal superhydrides. (see Manuscript File for full figure legend)

Supplementary Files

This is a list of supplementary files associated with this preprint. Click to download.

- ChemicalTemplateSuperhydridesSI.pdf